



Enhanced interfacial contact of dopamine bridged melamine-graphene/TiO₂ nano-capsules for efficient photocatalytic degradation of gaseous formaldehyde

Meiping Zhu^a, Yaseen Muhammad^{a,d}, Peng Hu^a, Bingfeng Wang^b, Yang Wu^a, Xiaodan Sun^a, Zhangfa Tong^{a,c}, Zhenxia Zhao^{a,c,*}

^a Guangxi Key Laboratory of Petrochemical Resource Processing and Process Intensification Technology, Guangxi University, Nanning 530004, China

^b Department of Applied Chemistry, College of Materials and Energy, South China Agricultural University, Guangzhou 510642, China

^c Guangxi Colleges and Universities Key Laboratory of New Technology and Application in Resource Chemical Engineering, Guangxi University, Nanning 530004, China

^d Institute of Chemical Sciences, University of Peshawar, 25120 KP, Pakistan

ARTICLE INFO

Keywords:

Melamine-graphene/TiO₂ nano-capsule
Enhanced interfacial contact
Photocatalytic degradation
Gaseous formaldehyde
DFT simulation

ABSTRACT

A novel synergistic strategy of N-doping and N-wrapping/bridging to synthesize photosensitive and conductive Graphene-TiO₂ composite nano-capsules for gaseous HCHO degradation was proposed. High HCHO photo-degradation activity of the composite was attributed to the enhanced interfacial contact of TiO₂ with conductive melamine-doped graphene (MG) sheets by dopamine (DA) bridging. MG improved the electrical conductivity and photoinduced charges separation/transfer in the MG/TiO₂ composite. Moreover, hydrogen treated DA wrapped/bridged MG/TiO₂ composite (H-TiO₂@MG-D) forming a 3D nano-capsule structure, which could concomitantly strengthen the interfacial contact between TiO₂ and MG sheets and accelerates electron mobility. Characterization and DFT simulation results revealed that H-TiO₂@MG-D nano-capsules exhibited the lowest band gap (2.49 eV) and highest charges separation efficiency. Simulation results further indicated that N-doping accelerated the transfer of adsorption sites from acidic Ti⁴⁺ (for HCHO) to basic N sites (for HCOOH and CO₂) before and after HCHO degradation reaction. The enhanced interfacial contact of H-TiO₂@MG-D resulted in its remarkably higher HCHO photocatalytic degradation efficiency ($\eta = 92\%$) and fast degradation rate ($k = 15.04 \times 10^{-3} \text{ min}^{-1}$) than that of pristine TiO₂ by a factor of 4.1 and 9.2, respectively. Therefore, the present study attributed to ease of synthesis and novel N-doping and N-wrapping strategy for the preparation of highly conductive MG-TiO₂ composite can be deemed as an effective and promising pathway for HCHO photodegradation and other similar photocatalytic applications.

1. Introduction

Volatile organic compounds (VOCs) are troublesome air pollutants due to their role in the formation of photochemical ozone and smog, which pose potential threats to environment and human health [1]. They are carbon-based compounds with high vapor pressure, generally originating from industrial gaseous emissions, building materials and vehicular emissions. Among these, formaldehyde is a typical hazardous indoor pollutant and contributor to “sick building syndrome” [2]. Prolonged exposure to formaldehyde even at low concentrations causes nasal tumors, skin irritation and nasopharyngeal cancer [3]. Attributed to these hazards, increasing stringent regulations and public concerns have triggered for advanced abatement strategies for formaldehyde from indoor air [4], which include adsorption [5], bio-filtration [6],

condensation [7] and photocatalysis [8]. Among these approaches, photocatalysis is recognized highly effective and promising credited to its cost effectiveness, high-efficiency, and renewable and green nature [9]. In this regard, semi-conductive TiO₂ has performed well having these properties along with its chemical stability against photochemical corrosion [10]. However, the fast recombination of photo-induced electron/hole (e^-/h^+) within TiO₂ leads to its low quantum efficiency, hence hindering its practical applications [11,12]. Numerous efforts such as doping with non-metallic atoms e.g. C, N, S [13], introducing vacancies (Ti³⁺) into TiO₂ lattice [14], and coupling with co-catalysts (metal or carbonaceous materials) [15], have been adopted to circumvent these obstacles.

N-doped TiO₂ composite application has been considered one of the major strategies for enhancing photocatalytic activity of TiO₂. H. Diker

* Corresponding author at: Guangxi Key Laboratory of Petrochemical Resource Processing and Process Intensification Technology, Guangxi University, Nanning 530004, China.
E-mail address: zhaozhenxia@gxu.edu.cn (Z. Zhao).

et al. [16] prepared a series of N-doped TiO_2 from various N sources which attributed increased electrical conductivity displayed higher photocatalytic activity for methylene blue than pure TiO_2 . However, N-doped TiO_2 suffered from insufficient charge separation resulting in photoelectron recombination and decreased photocatalytic activity [17]. Recently, graphene sheets have been proven as an effective substrate for facilitating electrons accepting and migration due to its conductive two dimensional (2D) network, large theoretical surface area ($\sim 2600 \text{ m}^2/\text{g}$) and flexible structure [18,19]. Pei et al. proposed the fabrication of coupled TiO_2/N -graphene composite with enhanced electron transfer ability, lower photoluminescence (PL) and 3.7 times higher H_2 evolution than pure TiO_2 [20]. Xue et al. prepared $\text{CdIn}_2\text{S}_4/\text{rGO}$ nanosheet arrays from reduced graphene oxide (rGO) as conductive substrate, which exhibited ~ 10 times higher H_2 evolution photocatalytic activity than nascent CdIn_2S_4 . This is attributed to the key role of rGO which not only facilitates the light-harvesting but also results in more exposed catalytic active sites [21] due to large surface area. Still, graphene hybrid photocatalysts suffer from weak interfacial contact and long-distance electrons transport between catalytic active centers and graphene substrate sheet, leading to the sluggish charges separation [22].

Pioneering attempts have been devoted to overcome these drawbacks including building “bridge” bonding [19], reconstructing unique nanostructure and charge transfer nanochannels [23,24]. Lin et al. [25] has constructed a novel g- C_3N_4 with 3D ordered macroporous architecture (3DOM g- C_3N_4) which could effectively create numerous migration channels for charges, resulting in dramatically enhanced RhB photodegradation activity of 3DOM g- C_3N_4 (~ 5.3 times higher than common 2D lamellar g- C_3N_4). Therefore, a concept of N wrapping TiO_2 nanoparticles anchoring on N doped graphene substrate and construct a 3D nano-capsule was proposed. N wrapping could not only produce 3D adsorption and conductive active sites, but also act as “bridge” linking and strengthening contact between TiO_2 nanoparticles and N-graphene substrate. To the best of our knowledge, there are rare reports on preparing 3D nano-capsule with enhanced interfacial contact based on N wrapping/bridging strategy.

Herein, a novel strategy based on concomitant N-doping and N-wrapping/bridging is applied to fabricate a photosensitive and highly conductive melamine-graphene/ TiO_2 nano-capsule. The resulting nano-capsule exhibited high photodegradation activity for HCHO due to improved electrical conductivity and enhanced interfacial contact between TiO_2 and MG sheets. Nano-structured TiO_2 was firstly *in situ* grown on MG nano-sheets support, followed by wrapping with DA nano-layer. DA could serve as a bridged-film concurrently linking TiO_2 and MG to form MG/ TiO_2 nano-capsule followed by hydrogen treatment (H- $\text{TiO}_2@\text{MG-D}$). The synergistic effect of N-doping and N-wrapping/bridging in H- $\text{TiO}_2@\text{MG-D}$ on chemical properties and photocatalytic degradation of gaseous HCHO at room temperature were investigated, and a reaction mechanism was proposed based on Gas Chromatography (GC) analysis. To the best of our knowledge, this is the first report on the applications of TiO_2 -MG composite for the photocatalytic degradation of gaseous HCHO.

2. Experimental

2.1. Materials and methods

All the chemicals used in this study were of analytical reagent grade and used without further purification. Dopamine hydrochloride ($\text{C}_8\text{H}_{12}\text{ClNO}_2$, $> 98\%$), melamine ($\text{C}_3\text{H}_6\text{N}_6$, $> 98\%$), and tetrabutyl titanate ($\text{C}_{16}\text{H}_{36}\text{O}_4\text{Ti}$, $> 98\%$) were purchased from Sigma, USA. Absolute ethanol ($\text{C}_2\text{H}_5\text{OH}$, 99.7%), and hexamethyl tetramine ($\text{C}_6\text{H}_{16}\text{N}_4$, $> 98\%$) were purchased from Kelong Chemical Reagent Co., Ltd. Chengdu, China. Natural graphite flake (7–10 nm) was purchased from JCNANO Co., Ltd. Nanjing, China.

2.2. Synthesis of catalysts

2.2.1. Synthesis of TiO_2 nanosphere

0.8 mL tetrabutyl titanate was dissolved in 20 mL absolute ethanol at room temperature, which was dropwise added to 45 mL deionized water under vigorous stirring for 1.5 h. The suspension was transferred into a 100 mL Teflon-lined autoclave, sealed and heated to 180°C for 10 h. After completion of reaction, the resulting product was centrifuged and rinsed with water several times. The pale yellow precipitate was dried at 60°C under vacuum and denoted as TiO_2 .

2.2.2. Synthesis of TiO_2 -graphene composite ($\text{TiO}_2@\text{G}$)

Graphene oxide (GO) was prepared and purified via modified Hummer's method [26]. Natural graphite flake was oxidized by concentrated H_2SO_4 , NaNO_3 and KMnO_4 . The GO powder was achieved by centrifugation followed by washing and drying. Finally, GO aqueous solution ($\sim 5 \text{ mg/mL}$) was obtained by ultrasonic dispersion (35 kHz and 1500 W) of GO powder in distilled water for 30 min.

5 mL GO solution (5 mg/mL) was dispersed in 35 mL deionized water under ultrasonication in an ice bath for 30 min. 0.8 mL tetrabutyl titanate was dissolved in 20 mL absolute ethanol and added dropwise to the above solution under vigorous stirring for 1.5 h. The mixture was transferred into a 100 mL Teflon-lined autoclave, sealed, and heated at 180°C for 10 h. After cooling the autoclave to room temperature, the product was centrifuged and rinsed with water several times. After freeze drying for 48 h, the black powder was obtained and denoted as $\text{TiO}_2@\text{G}$ composite.

2.2.3. Synthesis of TiO_2 -melamine/graphene composite ($\text{TiO}_2@\text{MG}$)

0.397 mmol melamine was added into the mixture of 5 mL GO aqueous solution (5 mg/mL) and 35 mL deionized water with ultrasonic-assisted dispersion in an ice bath for 30 min. Then, at 5000 rpm stirring, the mixture of tetrabutyl titanate (0.8 mL) and 20 mL absolute ethanol was dropwise added to the above solution. After stirring for 1.5 h, the solution was heated in 100 mL Teflon-lined autoclave at 180°C for 10 h. The autoclave was cooled down and the black powder $\text{TiO}_2@\text{MG}$ was obtained by centrifugation, water rinsing and freeze drying.

2.2.4. Synthesis of $\text{TiO}_2@\text{MG-D}$ nano-capsules

The resulting suspension of $\text{TiO}_2@\text{MG}$ (Section 2.2.3) was poured into a beaker and vigorously stirred for 10 min. Then, 0.1 g hexamethyl tetramine was added and stirred for 20 min followed by addition of dopamine hydrochloride solution (0.634 mmol in 5 mL deionized water). The mixture was transferred into a 100 mL Teflon-lined autoclave, sealed and heated at 90°C for 3 h. After cooling the autoclave, the black product was obtained by centrifugation, washing and drying, which was denoted as $\text{TiO}_2@\text{MG-D}$.

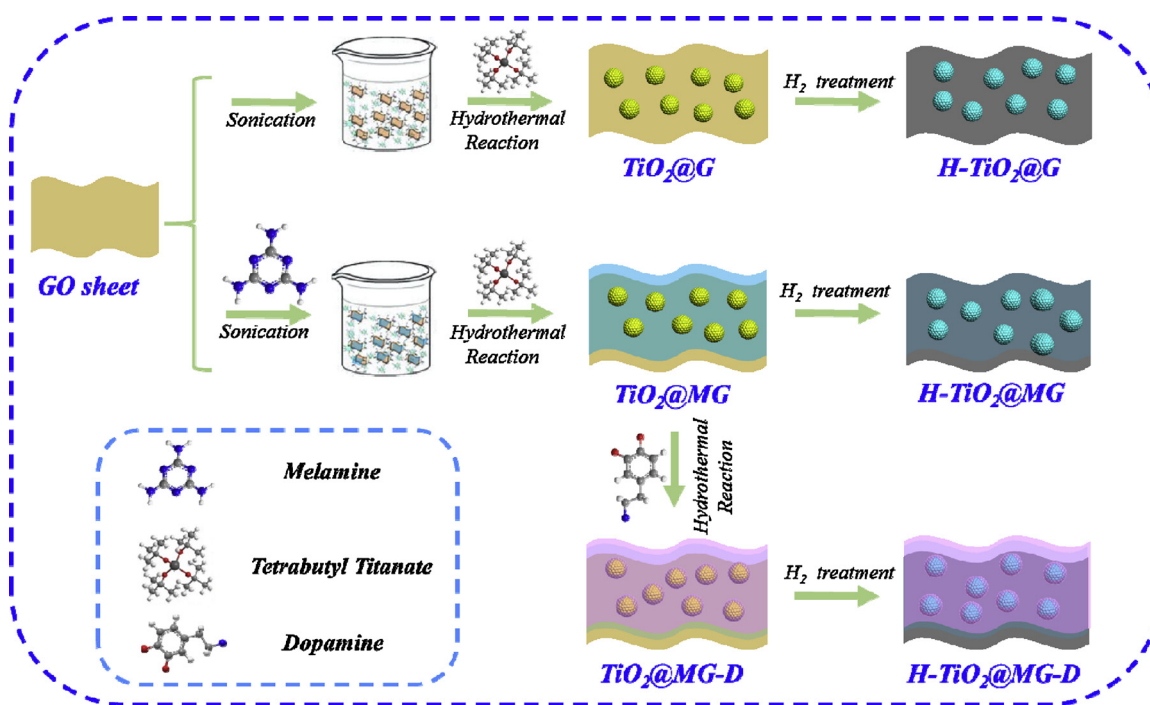
2.2.5. Procedure for hydrogen treatment

Four hydrogen-treated samples (H- TiO_2 , H- $\text{TiO}_2@\text{G}$, H- $\text{TiO}_2@\text{MG}$ and H- $\text{TiO}_2@\text{MG-D}$) were prepared by annealing TiO_2 , $\text{TiO}_2@\text{G}$, $\text{TiO}_2@\text{MG}$ and $\text{TiO}_2@\text{MG-D}$ at 300°C for 2 h at a heating rate of $5^\circ\text{C}/\text{min}$ in 80 mL ($\text{H}_2/\text{N}_2 = 1:9$ mixture), respectively.

A schematic representation of synthesis procedure of $\text{TiO}_2@\text{G}$, $\text{TiO}_2@\text{MG}$ and $\text{TiO}_2@\text{MG-D}$ and their hydrogenated samples is shown in Scheme 1.

2.3. Textural characterizations

Morphologies and microstructures of prepared samples were characterized by field-emission scanning electron microscopy (FESEM, SU8020, Hitachi, Japan) and transmission electron microscopy (TEM, FEI TECNAI G2 F30, USA) with 300 kV acceleration voltage. Crystalline structure was determined by a Rigaku X-ray diffraction (XRD, Smart Lab diffractometer, Japan, Cu K α radiation at 30 kV) and Raman



Scheme 1. Schematic representation of synthesis procedure of $\text{TiO}_2@\text{G}$, $\text{TiO}_2@\text{MG}$ and $\text{TiO}_2@\text{MG-D}$ and their hydrogenated versions.

spectroscopy (LabRAM HR Evolution, France) equipped with a 532 nm laser. Functional group identification was achieved using Nicolet 6700 Fourier transform infrared spectrometer (FT-IR, Thermo Fisher Scientific) via KBr disc method. Langmuir and Branauer-Emmett-Teller (BET) specific surface area (SSA) and pore size distribution (PSD) were measured using ASAP 2020 accelerated surface area and porosimetry system (Micromeritics, USA) at 77 K via degassing samples at 423 K for 6 h by inert gas to remove any moisture and impurities. UV–vis diffuse reflectance spectra (DRS) were obtained using a UV–vis spectrophotometer (TU-1900, Beijing Persee General Instrument Co., Ltd.). PL spectral analysis was performed with a luminescence fluorescence spectrophotometer (ZLX-PL-I, Beijing Zolix Co., Ltd.) at an excitation wavelength of 325 nm. Electron Spin Resonance (ESR) spectra were conducted on an ESR spectrometer (JEOL, Tokyo, Japan).

2.4. Photocatalytic activity measurements

The photocatalytic degradation of gaseous HCHO was performed in a closed quartz glass jar micro-reactor (350 mL) under UV irradiation at room temperature in wavelength range of 250–380 nm (controlled by UVREF filter). UV light was provided by a simulated solar light source (300 W Xe lamp, PLS-SXE300UV, Beijing Perfectlight. Co.). Firstly, 0.1 g catalyst was placed on a sample stand at a distance of ~10 cm from light source. Gaseous HCHO (~200 ppm) was fed into the reactor for 7 min at 50 mL/min followed by photocatalytic measurement under UV irradiation. HCHO concentration in the system was determined at an interval of 30 min using a gas chromatograph (GC) (Agilent 7820 A) equipped with a flame ionization detector (FID). Formaldehyde degradation efficiency (η , %) was determined using Eq. (1) [27]:

$$\eta = \frac{(C_0 - C)}{C_0} \times 100\% \quad (1)$$

Where C_0 and C stand for the concentration of initial and remaining formaldehyde, respectively.

2.5. Parameter and process simulation

Simulations for the photocatalytic process were achieved by using

Materials Studio with building in Materials Visualizer module, while calculation and analysis were completed in CASTEP module [28,29]. CASTEP module uses density functional theory (DFT) of quantum mechanics, where total energy function is comprised of numerical wavefunction of atomic orbitals [29]. DFT calculations were utilized to explore the energy band gap of intrinsic TiO_2 , N-doped as well as H_2 -reduced N-doped TiO_2 ($\text{H-TiO}_2@\text{MG-D}$) for better understanding their physico-chemical characteristics.

In the process of model construction and analysis, firstly, optimized models of intrinsic anatase TiO_2 (001) perfect surface were constructed [28], followed by replacing an oxygen atom with nitrogen at the surface of anatase TiO_2 (001) to form two-defected TiO_2 . Subsequently, geometry optimization was carried out to establish closest possible resemblance between parameters of the models with real molecules. General gradient approximate (GGA) with high precision was used to measure energy band gaps of three types of TiO_2 . The interaction effect of electrons was completed by Perdew Burkeand Ernzerhof (PBE) function [30]. For more precise calculations, double numeric basis with polarization (DNP) was also used to calculate the atomic orbitals with the fitting of d and p orbital polarization functions. The brillouin k-points were sampled on a G-centred Monkhorst-Pack grid of $3 \times 3 \times 1$ for the unit cell and the geometry was allowed to relax until Hellmann-Feynman force on each atom was less than $0.03 \text{ eV}/\text{\AA}$. Energy convergence precision was set at $1.0 \times 10^{-5} \text{ Ha}$, with energy gradient of $0.002 \text{ Ha}/\text{\AA}$, atom displacement of 0.005 \AA , and charge density convergence accuracy of self-consistent field of $1.0 \times 10^{-6} \text{ Ha}$ [28]. The calculation also took the dispersion force or van der Waals interactions into consideration by using semi-empirical DFT-D (Grimme) approaches.

3. Results and discussion

3.1. Textural characterization of TiO_2 and N-doped TiO_2 composites

3.1.1. Characterization of TiO_2 nanosphere

SEM images of TiO_2 , $\text{TiO}_2@\text{G}$, $\text{TiO}_2@\text{MG}$, $\text{TiO}_2@\text{MG-D}$ shown in Fig. 1 suggest that pristine TiO_2 (Fig. 1a) exhibited irregular nanospheres with particle size of ~20 nm. After adding GO, $\text{TiO}_2@\text{G}$ (Fig. 1b) displayed a 3D layer-stacked structure, which was different

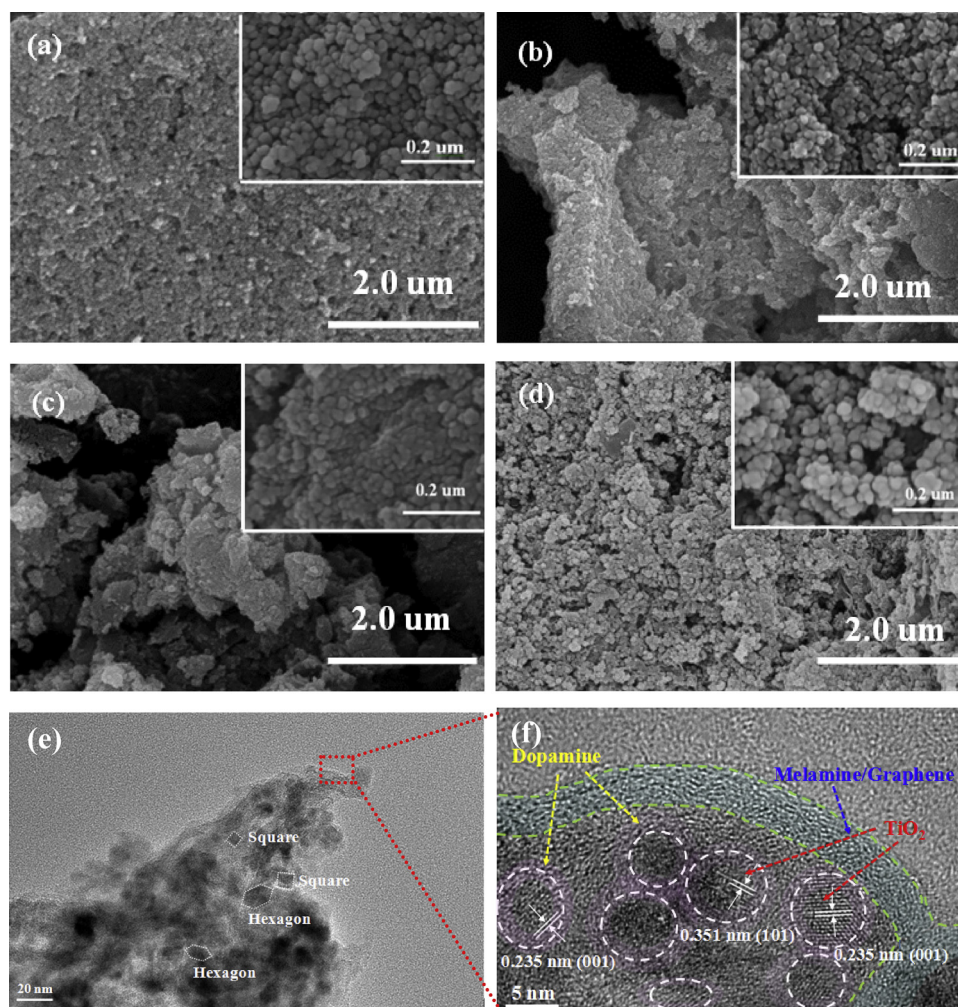


Fig. 1. SEM images of: (a) TiO_2 , (b) $\text{TiO}_2@\text{G}$, (c) $\text{TiO}_2@\text{MG}$ and (d) $\text{TiO}_2@\text{MG-D}$, (e) HRTEM images of $\text{TiO}_2@\text{MG-D}$, (f) enlarged view of the selected area in (e). The insets of (a–d) show the corresponding enlarged view of SEM images.

from pure GO having 2D nano-sheet connected networks (Fig. S2). A zoomed image of Fig. 1b shows that highly dispersed TiO_2 nanocrystals anchored on the surface of GO sheets. Moreover, the size of TiO_2 particles in the $\text{TiO}_2@\text{G}$ (~ 10 nm) was significantly smaller than that in pure TiO_2 (~ 20 nm). Similar morphology and particle size were observed in $\text{TiO}_2@\text{MG}$ (Fig. 1c), indicating minimal effect of melamine doping on particle size of TiO_2 nanospheres. Furthermore, DA incorporated $\text{TiO}_2@\text{MG}$ i.e. $\text{TiO}_2@\text{MG-D}$ (Fig. 1d) showed numerous nanoparticles adhering to nano-sheet connected networks where TiO_2 nanoparticles exhibited larger particle size than those in $\text{TiO}_2@\text{MG}$ and $\text{TiO}_2@\text{G}$. This could be attributed to DA coating wrapped around TiO_2 nanoparticles [31].

High-resolution TEM (HRTEM) images of $\text{TiO}_2@\text{MG-D}$ nano-capsules are depicted in Fig. 1e and f, where the former shows a well-covered MG sheets with numerous TiO_2 nanoparticles and the latter evidenced the edge of TiO_2 and MG sheets. Furthermore, the enlarged view (Fig. 1f) of red frame in Fig. 1e revealed that the clear lattices fringe spacing in $\text{TiO}_2@\text{MG-D}$ nano-capsules were ~ 0.351 and 0.235 nm, assigned to (101) and (001) planes of anatase TiO_2 , respectively [32]. TiO_2 wrapped by DA showed a very small dimension of 5–10 nm with uniform isolation of amorphous layer. The enhanced adherence of TiO_2 particles with MG sheets *via in situ* growth strategy and DA bridged-film can inhibit agglomeration of original TiO_2 crystals, which resulted in dramatic decrease of TiO_2 particles dimension [33]. This extremely small size of TiO_2 crystal in $\text{TiO}_2@\text{MG-D}$ would result in size-dependent quantization effects [34].

Meanwhile, the homogeneous distribution of C, N, O and Ti in $\text{TiO}_2@\text{MG-D}$ shown in Fig. S3 is credited to the high dispersion of TiO_2 nanoparticles. SEM and TEM results concluded that a close interfacial contact of TiO_2 with MG and DA was formed in $\text{TiO}_2@\text{MG-D}$ composite with a nano-capsule structure, which is beneficial for efficient charge carrier transfer and separation in photo-catalysis [35].

3.1.2. Crystal structural characterization

The XRD patterns shown in Fig. 2 suggest similar diffraction peaks of H_2 reduced TiO_2 composites to those of pure TiO_2 located at 25.1° , 38.0° , 48.0° , 54.6° , 62.8° , 69.0° , 75.0° and 82.9° , indexed to (101), (004), (200), (211), (220), (204), (215) and (224) crystal planes attributed to typical anatase phase of TiO_2 (JCPDS 21-1272) [36], respectively. This shows the minimal effect of dopants (GO/melamine/DA) on the alteration of crystal phase of TiO_2 under current experimental conditions [37].

In addition, weaker intensity of main peak (101) in H- TiO_2 compared with that of pristine TiO_2 could be attributed to the formation of defects in their lattices by hydrogenation [11], which plays an important role in photocatalytic activity.

3.1.3. Raman spectra

Raman spectra, further describing the structural properties of pristine TiO_2 and its composites, are shown in Fig. 3a. Pure TiO_2 and H- TiO_2 exhibited four peaks at ~ 150 cm^{-1} ($\text{E}_{\text{g}(1)}$), 396 cm^{-1} ($\text{B}_{1\text{g}}$), 514 cm^{-1} ($\text{A}_{1\text{g}}$) and 639 cm^{-1} ($\text{E}_{\text{g}(2)}$) ascribed to pure anatase TiO_2 [27].

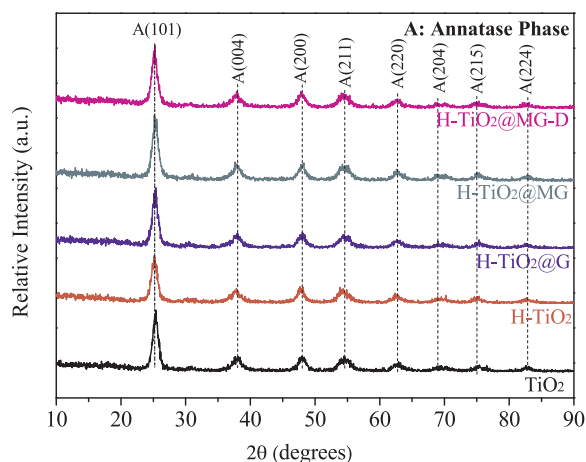


Fig. 2. XRD patterns of TiO_2 , H-TiO_2 , $\text{H-TiO}_2@\text{G}$, $\text{H-TiO}_2@\text{MG}$ and $\text{H-TiO}_2@\text{MG-D}$.

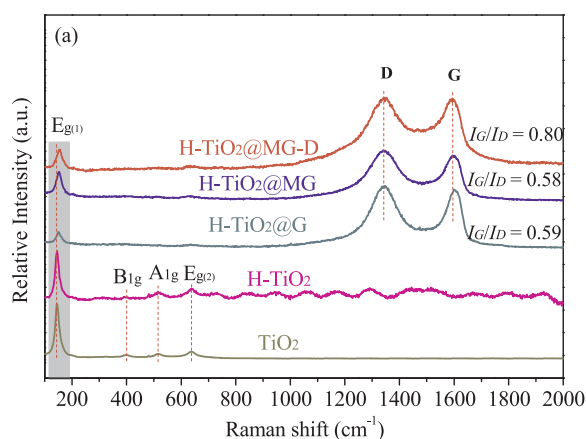


Fig. 3. (a) Raman spectra of TiO_2 , H-TiO_2 , $\text{H-TiO}_2@\text{G}$, $\text{H-TiO}_2@\text{MG}$, $\text{H-TiO}_2@\text{MG-D}$, (b) An enlarged view of the main $\text{E}_{\text{g}(1)}$ in (a).

Two typical peaks at 1347 cm^{-1} and 1595 cm^{-1} classified as D band (broad disorder-induced) and G band (in-plane vibration) were observed in $\text{H-TiO}_2@\text{G}$, $\text{H-TiO}_2@\text{MG}$ and $\text{H-TiO}_2@\text{MG-D}$ composites [38], which confirmed the successful incorporation of TiO_2 and carbon matrices [40].

Additionally, the main $\text{E}_{\text{g}(1)}$ mode of H-TiO_2 weakened and exhibited slight blue-shift compared to that of pristine TiO_2 (Fig. 3b) and may be ascribed to the formation of oxygen vacancies after hydrogen treatment [39], which was in good agreement with XRD results (Fig. 2). Moreover, the main $\text{E}_{\text{g}(1)}$ peaks of TiO_2 composites were further broadened and blue-shifted after TiO_2 coupling with dopants (GO/

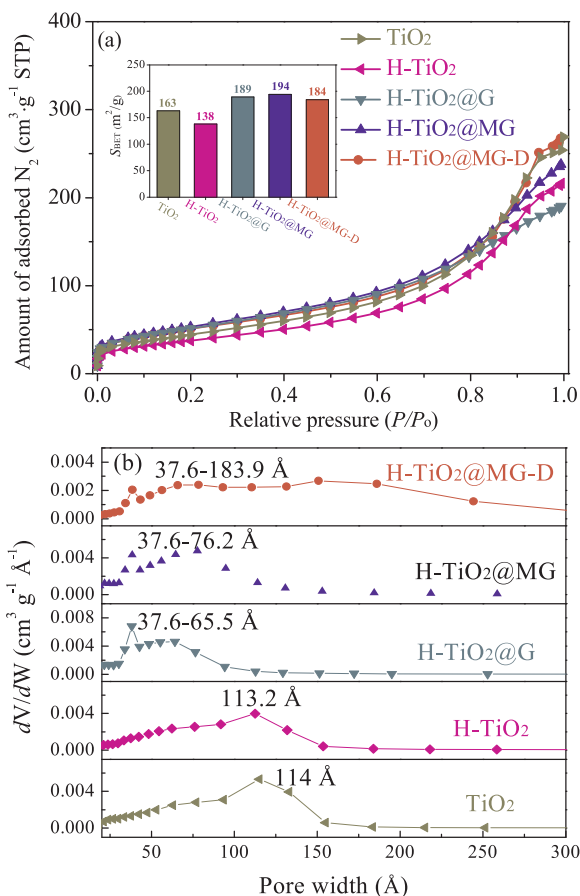


Fig. 4. (a) Nitrogen adsorption isotherms and (b) Pore size distribution of TiO_2 , H-TiO_2 , $\text{H-TiO}_2@\text{G}$, $\text{H-TiO}_2@\text{MG}$ and $\text{H-TiO}_2@\text{MG-D}$ using BJH model. Inset of (a) shows BET surface area for all samples.

melamine/DA), which was due to high dispersion and decreased crystal size of TiO_2 [43]. It was in good agreement with the SEM results (Fig. 1). In addition, the $I_{\text{G}}/I_{\text{D}}$ value of $\text{H-TiO}_2@\text{G}$, $\text{H-TiO}_2@\text{MG}$, $\text{H-TiO}_2@\text{MG-D}$ were estimated to be 0.59, 0.58, 0.80, respectively, which indicated the highest graphitization degree of $\text{H-TiO}_2@\text{MG-D}$ credited to the outer nano-layer of DA [41]. This could play crucial role in improving the electrical conductivity as well as electron mobility of $\text{H-TiO}_2@\text{MG-D}$, which could effectively restrict photoelectron-hole recombination [42].

N_2 adsorption-desorption isotherms of TiO_2 and its composites depicted in Figs. 4 and S4 were close to typical type IV with H1 hysteresis loop, suggesting the existence of mesoporous structure, while SSA of TiO_2 , H-TiO_2 , $\text{H-TiO}_2@\text{G}$, $\text{H-TiO}_2@\text{MG}$ and $\text{H-TiO}_2@\text{MG-D}$ was 163, 138, 189, 194 and 184 m^2/g , respectively (inset of Fig. 4a). It is noted that SSA of H-TiO_2 slightly decreased after hydrogen treatment at 300°C , which could be attributed to TiO_2 nanoparticles growth due to slight sintering and agglomeration around TiO_2 shell [44]. In addition, the SSA of all graphene-containing composites increased dramatically compared to that of pristine TiO_2 , which could be attributed to graphene support with large theoretical SSA of $\sim 2600\text{ m}^2/\text{g}$ [45]. Furthermore, the marginal decrease in SSA of $\text{H-TiO}_2@\text{MG}$ could be due to thick layer of DA around TiO_2 nano-particle. It is believed that DA should be wrapped as thin layer rather a dense one, where the latter leads to ultralow SSA ($13.1\text{ m}^2/\text{g}$) of polymerized DA [46] would dramatically decrease the surface area of the whole TiO_2 composites.

The PSD curves (Fig. 4b) obtained from the desorption branch of isotherms in Fig. S4 using Barrett-Joyner-Halenda (BJH) method suggest similar PSD curves of pure TiO_2 and H-TiO_2 centered at $\sim 11.3\text{--}11.4\text{ nm}$. After incorporating GO and MG sheets onto TiO_2 , pore

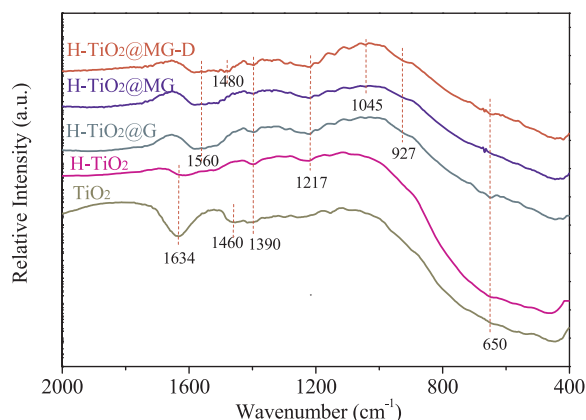


Fig. 5. FTIR spectra of TiO_2 , H-TiO_2 , $\text{H-TiO}_2@\text{G}$, $\text{H-TiO}_2@\text{MG}$ and $\text{H-TiO}_2@\text{MG-D}$.

size of $\text{H-TiO}_2@\text{G}$ and $\text{H-TiO}_2@\text{MG}$ decreased, and then increased with DA coating in $\text{H-TiO}_2@\text{MG-D}$ capsule structure.

The FTIR spectra of samples are depicted in Fig. 5. For pure TiO_2 , the bands located at $400\text{--}800\text{ cm}^{-1}$ were attributed to Ti-O and Ti-O-Ti stretching vibration [11]. The peaks located at 1634 , 1460 , and 1390 cm^{-1} were assigned to -OH distorting vibration due to physisorbed water [27], C-O stretching [47] and Ti-O stretching vibration [27], respectively. Compared with the original TiO_2 , H-TiO_2 exhibited weaker -OH groups (1634 cm^{-1}) and disappearance of C-O stretching (1460 cm^{-1}). Besides, a new peak at 1217 cm^{-1} ascribed to C-OH stretching vibration appeared [27]. These results indicated that H-TiO_2 was reduced by high temperature hydrogenation. In comparison to H-TiO_2 , $\text{H-TiO}_2@\text{G}$ displayed two new peaks at 1560 and 927 cm^{-1} , corresponding to aromatic C=C from rGO sheets [48] and Ti-O-C bond stretching vibrations [49], respectively. This confirmed the successful coupling of rGO sheets with TiO_2 via *in situ* hydrothermal treatment.

Moreover, after simultaneous addition of GO and melamine, two new peaks at 1560 and 1045 cm^{-1} assigned to C=C/C=N and C-N bonding [38], respectively, were observed. Furthermore, compared to $\text{H-TiO}_2@\text{MG}$, $\text{H-TiO}_2@\text{MG-D}$ exhibited a new peak at 1480 cm^{-1} attributed to -NH_2 of DA [50].

The surface chemical states and full survey spectra of $\text{H-TiO}_2@\text{MG}$ and $\text{H-TiO}_2@\text{MG-D}$ were probed by XPS and shown in Fig. 6. For comparison, the main element (Ti, O and N) contents in $\text{H-TiO}_2@\text{MG}$ and $\text{H-TiO}_2@\text{MG-D}$ detected by XPS and EDX are displayed in Figs. 7 and S5, respectively. An obvious difference in elemental distribution between composite surface (XPS depth: $< 5\text{ nm}$) [51] and bulk (EDX depth: $\sim 0.5\text{--}1\text{ }\mu\text{m}$) [52] indicated the heterogeneous structure of $\text{H-TiO}_2@\text{MG}$ and $\text{H-TiO}_2@\text{MG-D}$. XPS results showed that for $\text{H-TiO}_2@\text{MG}$

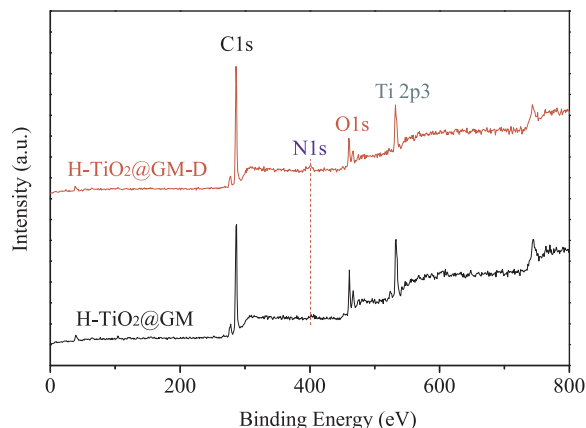


Fig. 6. XPS survey spectra of $\text{H-TiO}_2@\text{MG}$ and $\text{H-TiO}_2@\text{MG-D}$.

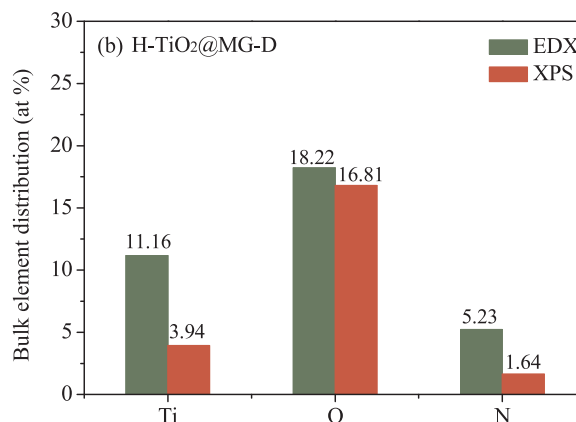
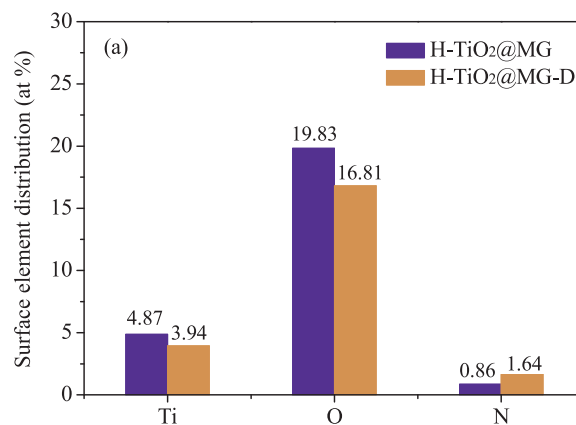


Fig. 7. (a) Surface element (Ti, O and N) distribution of $\text{H-TiO}_2@\text{MG}$ and $\text{H-TiO}_2@\text{MG-D}$ obtained from XPS, and (b) bulk and surface element (Ti, O and N) distribution of $\text{H-TiO}_2@\text{MG-D}$ obtained from EDX and XPS, respectively.

MG-D , the contents of surface Ti and O decreased, while surface N slightly increased compared to $\text{H-TiO}_2@\text{MG}$. This further confirmed the wrapping of N-containing DA around TiO_2 surface in $\text{H-TiO}_2@\text{MG-D}$ composite, and the nano-capsule structure was formed along with the MG sheets support.

3.1.4. Spectra analysis

High-resolution XPS spectra of C 1s, N 1s and Ti 2p for TiO_2 and its composites are illustrated in Figs. 8 and S6. In Fig. 8a, the C 1s spectra of $\text{H-TiO}_2@\text{G}$, $\text{H-TiO}_2@\text{MG}$ and $\text{H-TiO}_2@\text{MG-D}$ exhibited three peaks at 283.5 , 284.6 , 285.6 eV , corresponding to Ti-C [53], sp^2 -hybridized C [54], and sp^3 -hybridized C ($\text{sp}^3\text{ C}$ & C-N of $\text{H-TiO}_2@\text{MG}$ and $\text{H-TiO}_2@\text{MG-D}$) [55], respectively. Meanwhile, an additional peak at 287.0 eV ascribed to C=N groups appeared in both $\text{H-TiO}_2@\text{MG}$ and $\text{H-TiO}_2@\text{MG-D}$ samples [56,57]. This information confirmed the chemical reactions of C matrix (GO) with TiO_2 and N species (melamine or DA) under hydrothermal process.

Moreover, $\text{H-TiO}_2@\text{MG}$ and $\text{H-TiO}_2@\text{MG-D}$ displayed three peaks in N 1s spectra (Fig. 8b) at 398.6 , 400.0 and 401.2 eV , assigned to pyridinic N (C=N-C) [58], N-Ti-O or pyrrolic N (N-C_3) [59] and graphitic N (C-N-H) [60], respectively. This further confirmed that N element was doped into carbon matrix (GO nanosheets) and TiO_2 lattice via *in situ* hydrothermal reaction. The relative amount of different N species in $\text{H-TiO}_2@\text{MG}$ and $\text{H-TiO}_2@\text{MG-D}$ was measured from the peak area of N-binding configurations to total area as shown in Table 1. An increase in the amount of graphitic N and N-Ti-O/Pyrrolic N of $\text{H-TiO}_2@\text{MG-D}$ compared to $\text{H-TiO}_2@\text{MG}$ suggested that DA addition not only facilitated electric conductivity (graphitic N) [61], but also enhanced the interfacial interaction (N-Ti-O bonding) of $\text{H-TiO}_2@\text{MG-D}$ [62].

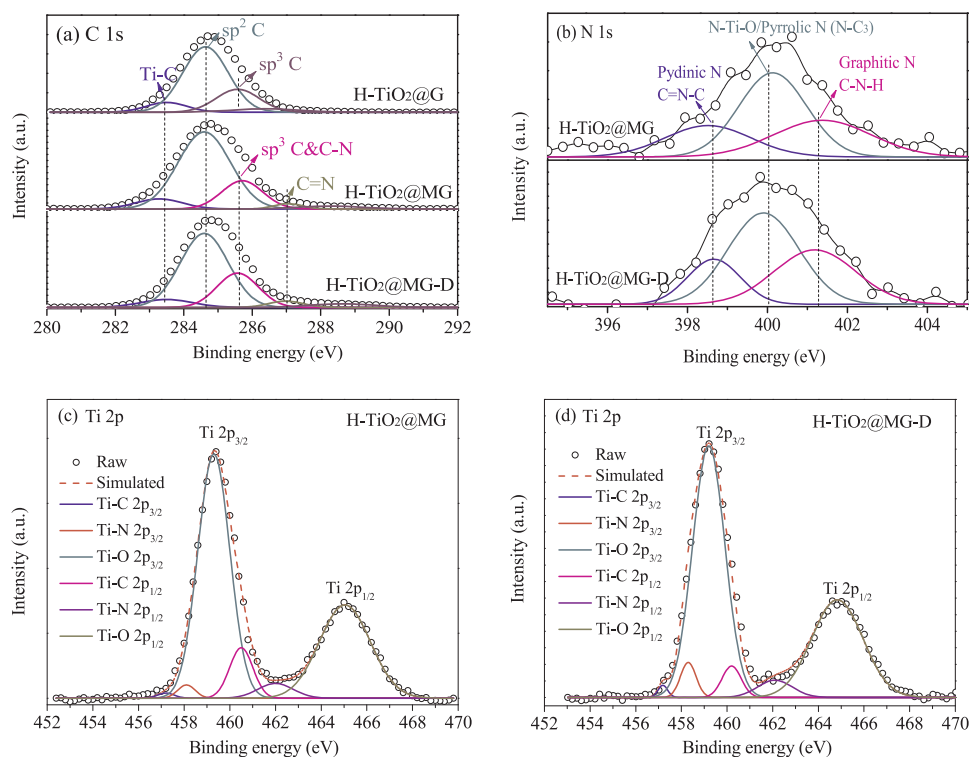


Fig. 8. High resolution XPS spectra of: (a) C 1s for H-TiO₂@G, H-TiO₂@MG and H-TiO₂@MG-D, (b) N 1s for H-TiO₂@MG and H-TiO₂@MG-D, Ti 2p for (c) H-TiO₂@MG and (d) H-TiO₂@MG-D.

Table 1
XPS peak area of various N-binding configurations to total area.

Sample	Percentage of N-binding Peaks to Total Area (TA, at%)		
	$A_{\text{(Pyridinic N)}}/TA^a$	$A_{\text{(N-Ti-O/Pyrrhic N)}}/TA^a$	$A_{\text{(Graphitic N)}}/TA^a$
H-TiO ₂ @MG	22.60	47.64	29.76
H-TiO ₂ @MG-D	17.86	48.84	33.30

^a A: area of single peak ; TA: total area of all peaks.

Furthermore, as shown in Figs. 8c, d and S6, the Ti 2p spectra of TiO₂ and its hybrids were split into two peaks centered at 459.3 and 465.0 eV, which were assigned to Ti 2p_{3/2} and Ti 2p_{1/2} [63], respectively. To better investigate the chemical nature of Ti 2p in these samples, Ti 2p spectra of pure TiO₂ and H-TiO₂ were deconvoluted into two peaks, which were assigned to Ti-O (2p_{3/2}) and Ti-O (2p_{1/2}) [64]. After coupling with GO, H-TiO₂@G exhibited two new peaks attributed to Ti-C (2p_{3/2}) and Ti-C (2p_{1/2}), confirming the successful coupling of TiO₂ and GO sheets. Compared with H-TiO₂@G, two new peaks attributed to Ti-N (2p_{3/2}) and Ti-N (2p_{1/2}) appeared in H-TiO₂@MG and H-TiO₂@MG-D, suggesting that some N from melamine or DA was chemically bonded to Ti in TiO₆ octahedron [11,65]. It would be conducive to improve the interfacial contact as well as photocatalytic activity of H-TiO₂@MG-D.

Details about the change in binding energy of various Ti-binding in terms of Ti-O (Ti-O 2p_{3/2} and Ti-O 2p_{1/2}) and Ti-N (Ti-N 2p_{3/2} and Ti-N 2p_{1/2}) peaks are provided in Table S1. The Ti-O binding energy of H-TiO₂ and TiO₂ were quite similar while it decreased in H-TiO₂@MG-D compared to that in H-TiO₂@MG. Additionally, H-TiO₂@MG and H-TiO₂@MG-D displayed positive shift in Ti-N binding energy compared to H-TiO₂. These results demonstrated that replacing -O by -N increased the electron density on Ti [66], which is beneficial for electron transfer from N to Ti [67].

Optical properties of TiO₂, H-TiO₂, H-TiO₂@G, H-TiO₂@MG and H-TiO₂@MG-D were measured using UV-vis DRS as shown in Fig. 9a.

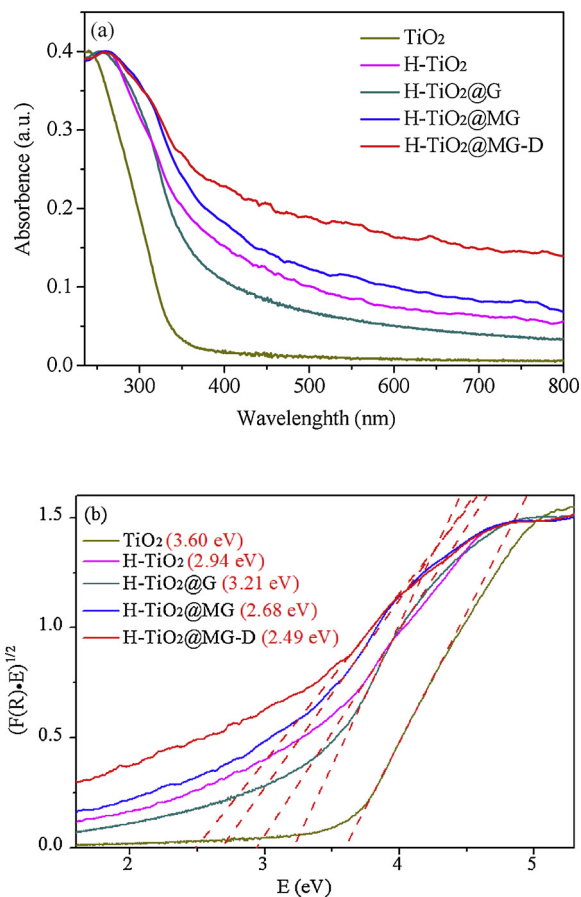


Fig. 9. (a) UV-vis DRS of TiO₂, H-TiO₂, H-TiO₂@G, H-TiO₂@MG and H-TiO₂@MG-D, (b) Plots of transformed Kubelka-Munk function vs. photon energy.

Pure TiO_2 and its composites exhibited pronounced absorption band in UV region of 250–400 nm, caused by electron excitation of TiO_2 semiconductor from valence band (VB) to conduction band (CB) [63], and a weak absorption at wavelengths longer than 500 nm, with adsorption edge at ~ 400 nm. In case of $\text{H-TiO}_2@\text{MG}$, the absorption edge was shifted to visible region (400–800 nm), which was further enhanced after coupling with melamine. The DA coated composite *i.e.* $\text{H-TiO}_2@\text{MG-D}$, exhibited a significant red-shift and stronger intensity in light absorption compared to $\text{H-TiO}_2@\text{MG}$, which was attributed to the wrapping of TiO_2 by DA nano-layer [31].

To further study the band gaps of TiO_2 and its composites, plots of transformed Kubelka-Munk function vs. photon energy are shown in Fig. 9b. In Fig. 9b, the band gaps of TiO_2 , H-TiO_2 , $\text{H-TiO}_2@\text{G}$, $\text{H-TiO}_2@\text{MG}$ and $\text{H-TiO}_2@\text{MG-D}$ were 3.60, 2.94, 3.21, 2.68 and 2.49 eV, respectively. H-TiO_2 displayed a 0.66 eV narrower band gap than pure TiO_2 due to the introduction of oxygen vacancies after hydrogenation. Compared with $\text{H-TiO}_2@\text{G}$, a 0.53 eV reduction in band gap of $\text{H-TiO}_2@\text{MG}$ was attributed to the chemical bonding between Ti and C or N on MG sheets [68]. Interestingly, the band gap of $\text{H-TiO}_2@\text{MG-D}$ was further reduced to 2.49 eV, which was probably due to enhanced and effective interfacial chemical interaction between MG and TiO_2 . It may be beneficial to improve the interfacial charges separation efficiency and mobility [32], as well as photocatalytic activity of $\text{H-TiO}_2@\text{MG-D}$.

To investigate the interfacial charge separation efficiency on photocatalyst surface, PL emission spectra were conducted with an excitation wavelength of 320 nm for all photocatalysts shown in Fig. 10. As shown in Fig. 10a, TiO_2 exhibited a strong peak at ~ 440 nm which was due to the easy recombination of photoinduced electrons and holes. After hydrogen treatment, a dramatic decrease in PL peak of H-TiO_2 was noted. It is believed that the formation of oxygen vacancies by hydrogen treatment could effectively hinder the recombination of electron-hole pairs [69]. Furthermore, as shown in Fig. 10b, in comparison to H-TiO_2 , the $\text{H-TiO}_2@\text{G}$ displayed minimal change in the PL intensity after graphene addition, which indicated a restricted interfacial migration of charge carriers between GO and TiO_2 [70]. This issue was minimized by the introduction of N (from melamine), which was visible by a further weaker PL intensity spectrum of $\text{H-TiO}_2@\text{MG}$ than $\text{H-TiO}_2@\text{G}$. This effect was further strengthened by the introduction of DA (PL spectrum of $\text{H-TiO}_2@\text{MG-D}$), which is due to the enhanced interfacial contact by DA bridging with the unsaturated Ti(IV) atoms of TiO_2 and MG support [71], as well as the improved electrical conductivity by N-doped MG support. These results demonstrated that N doping (melamine-doped graphene support) and N wrapping/bridging (DA wrapped TiO_2) strategy can concomitantly accelerate electron-hole pair separation and transfer between the interface of MG and TiO_2 [61].

The active oxygen species involved in the photocatalytic reaction *i.e.* $\cdot\text{O}_2^-$ and $\cdot\text{OH}$ radicals were measured by ESR spectroscopy as shown in Figs. S7 and Fig. 11. The $\cdot\text{O}_2^-$ and $\cdot\text{OH}$ radicals were trapped

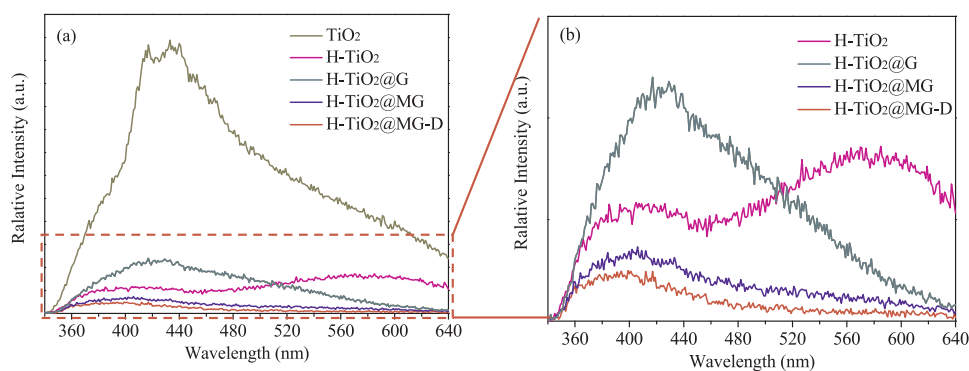


Fig. 10. (a) PL emission spectra of TiO_2 , H-TiO_2 , $\text{H-TiO}_2@\text{G}$, $\text{H-TiO}_2@\text{MG}$ and $\text{H-TiO}_2@\text{MG-D}$. (b) Zoomed view of samples without TiO_2 (red frame in (a)). (For interpretation of the references to colour in this figure legend, the reader is referred to the web version of this article).

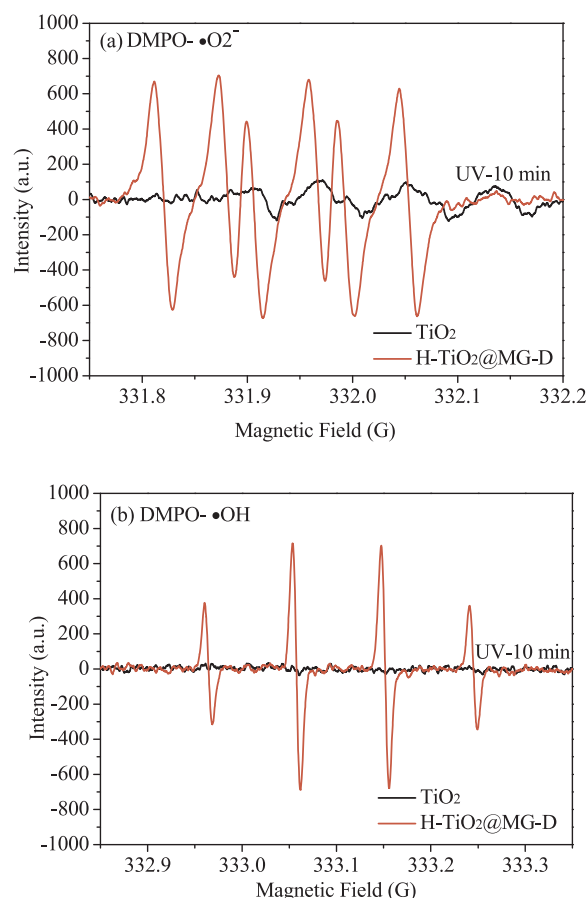


Fig. 11. ESR spectra of: (a) $\text{DMPO} \cdot \cdot\text{O}_2^-$ adducts in methanol suspension and (b) $\text{DMPO} \cdot \cdot\text{OH}$ adducts in aqueous suspension under UV irradiation for 10 min in TiO_2 and $\text{H-TiO}_2@\text{MG-D}$.

in methanol and aqueous suspensions by *N,N*-dimethyl pyrroline *N*-oxide (DMPO) under UV light irradiation. As shown in Fig. S7, almost no signals of $\cdot\text{O}_2^-$ and $\cdot\text{OH}$ in both TiO_2 and $\text{H-TiO}_2@\text{MG-D}$ were detected without light irradiation. After 10 min UV light exposure, the characteristic peaks of $\cdot\text{O}_2^-$ and $\cdot\text{OH}$ radicals appeared with a very weak intensity in pristine TiO_2 (Fig. S7a, b). It was attributed to the fast recombination and short lifetime of charge carriers in TiO_2 [68], as discussed in PL results.

For $\text{H-TiO}_2@\text{MG-D}$, $\cdot\text{O}_2^-$ was captured to form $\text{DMPO} \cdot \cdot\text{O}_2^-$ adduct with a quartet peak in methanol suspension (Fig. S7c), and a characteristic quartet peak of $\text{DMPO} \cdot \cdot\text{OH}$ adducts with intensity ratio of 1:2:2:1 was observed in Fig. S7d. The amount of $\cdot\text{O}_2^-$ and $\cdot\text{OH}$ species gradually increased with irradiation interval. Moreover, their intensity

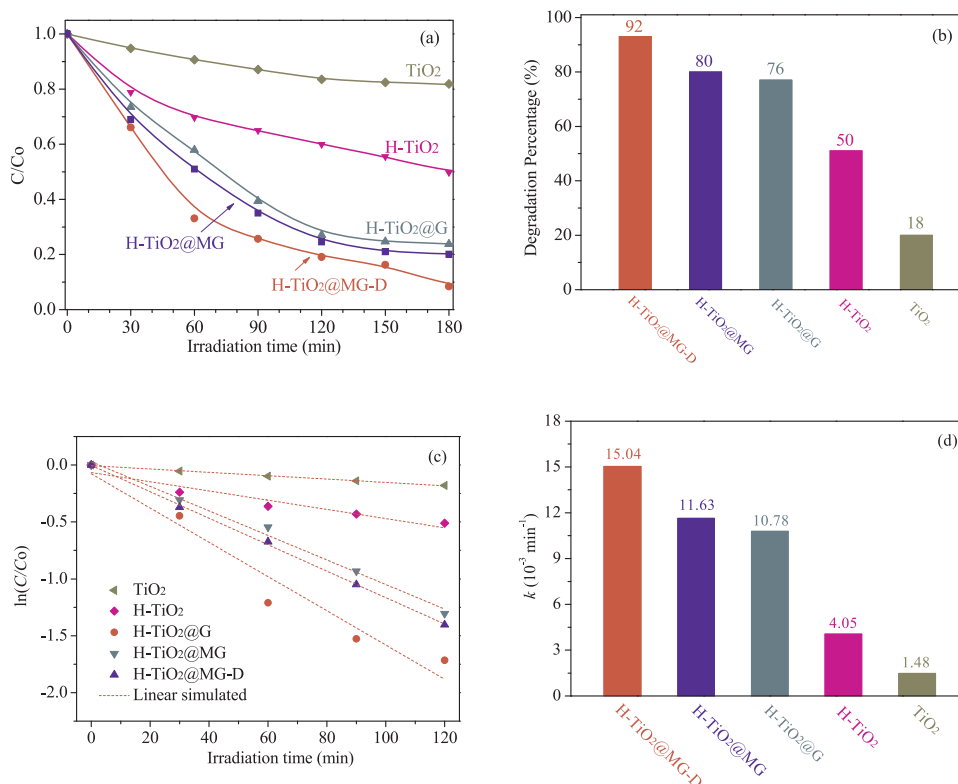


Fig. 12. (a) Photocatalytic degradation rate, (b) degradation activity, (c) pseudo-first-order kinetics curves of photocatalytic degradation and (d) Apparent reaction rate constants (k , min^{-1}) of gaseous HCHO over TiO_2 , H-TiO_2 , $\text{H-TiO}_2@\text{G}$, $\text{H-TiO}_2@\text{MG}$ and $\text{H-TiO}_2@\text{MG-D}$ under UV-irradiation.

was much stronger than that in pristine TiO_2 as shown in Fig. 11, indicating that more $\cdot\text{O}_2^-$ and $\cdot\text{OH}$ radicals were generated in $\text{H-TiO}_2@\text{MG-D}$. These results further confirmed an improved electron-hole separation efficiency of $\text{H-TiO}_2@\text{MG-D}$ compared with that of pristine TiO_2 .

3.2. Photocatalytic activity for gaseous HCHO degradation

Gaseous HCHO photocatalytic degradation activity results for pure TiO_2 and all synthesized composites are displayed in Fig. 12. The concentration of HCHO for all samples declined with increasing irradiation interval, and reached equilibrium after 180 min. As shown in Fig. 12b, the degradation efficiency increased from 18% (TiO_2) to 50% (H-TiO_2) by hydrogen treatment, attributed to the formation of oxygen vacancies which effectively inhibited charges recombination [72]. Similarly, $\text{H-TiO}_2@\text{G}$ composite exhibited 76% photocatalytic activity, about 26% higher than that of H-TiO_2 . This could be credited to the facile charge transportation and separation from TiO_2 to graphene with large π - π network [73]. Furthermore, the enhanced activity of $\text{H-TiO}_2@\text{MG}$ was related to the increase of graphitic-N and pyrrolic-N originated from melamine doped in graphene (Fig. 8b), which served as effective electron-transfer mediator and oxygen-reduction active site [61]. Besides, N doping would enhance the surface basicity of TiO_2 composite, and thus facilitates better adsorption and photo-degradation of HCHO [74] to CO_2 . Among all samples $\text{H-TiO}_2@\text{MG-D}$ ranked at the top of photocatalytic degradation activity (92%). This was attributed to the synergistic effect of N doping and N wrapping/bridging, where the former can improve electrical conductivity and affinity towards HCHO, while the later can enhance interfacial contact between TiO_2 and MG support, resulting in efficient electron transportation and minimized electron-holes recombination [32]. Apart from this, $\text{H-TiO}_2@\text{MG-D}$ photocatalyst exhibited high stability and minimal decrease in photocatalytic activity after four consecutive cycles (Fig. 13).

Moreover, pseudo-first order model was applied to investigate the

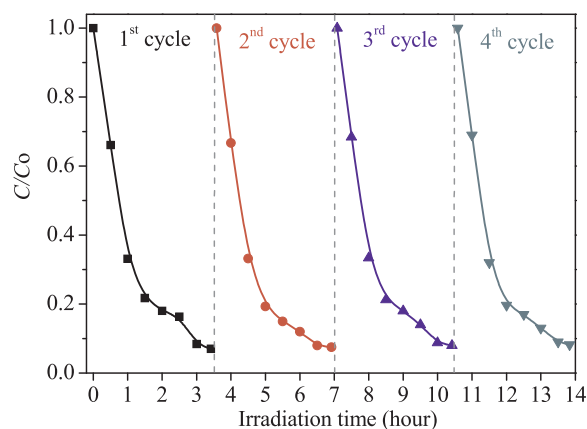


Fig. 13. Activity of $\text{H-TiO}_2@\text{MG-D}$ after four consecutive cycles in photocatalytic decomposition of HCHO under UV-irradiation.

kinetics of HCHO photocatalytic reaction over TiO_2 and its composites using Eq. (2):

$$\ln\left(\frac{C}{C_0}\right) = -kt \quad (2)$$

Where C/C_0 is the normalized concentration of HCHO, k is the apparent reaction rate constant (min^{-1}), and t is reaction time (min).

As seen in Fig. 12c, photocatalytic degradation curves fitted well with pseudo-first order model ($R^2 > 0.99$). The calculated rate constant value (k , 10^{-3} min^{-1}) of $\text{H-TiO}_2@\text{MG-D}$ in Fig. 12d was 15.04, which was 9.2, 2.7, 0.4 and 0.3 times higher than that of TiO_2 , H-TiO_2 , $\text{H-TiO}_2@\text{G}$ and $\text{H-TiO}_2@\text{MG}$, respectively. The high reaction rate by $\text{H-TiO}_2@\text{MG-D}$ was partly due to high dispersion of TiO_2 on graphene or MG support and large surface area due to coupling with graphene or MG sheets resulting in increased catalytic active sites HCHO interaction per unit time. Another reason could be the improved electrical

conductivity and enhanced interfacial contact between TiO_2 and MG sheets, which leads to higher charges separation efficiency and mobility on the interface of $\text{H-TiO}_2\text{@MG-D}$, generating more oxygen radicals around HCHO. In general, the synergistic effect of N-doping and N-wrapping/bridging in fabrication of $\text{H-TiO}_2\text{@MG-D}$ could simultaneously enhance its electrical conductivity, redox active sites, and adsorption affinity towards HCHO as well as charges separation efficiency. An overall HCHO degradation activity and reaction rate followed an order of: $\text{H-TiO}_2\text{@MG-D} > \text{H-TiO}_2\text{@MG} > \text{H-TiO}_2\text{@G} > \text{H-TiO}_2 > \text{TiO}_2$ (Table 3).

3.3. Nitrogen-doped anatase TiO_2 (001) surface and formaldehyde adsorption-degradation mechanism

3.3.1. Simulation structure of nitrogen-doped anatase TiO_2 (001) surface

Based on the aforementioned characterization results and discussion, the key to improved photocatalytic activity of $\text{H-TiO}_2\text{@MG-D}$ was assumed to be enhanced interfacial chemical interaction between MG and TiO_2 , which was caused by DA bridged-layer (~ 5 nm). This was attributed to the bridged layer of anatase TiO_2 which generated intra-band gap N related defects [29] and surface Ti^{3+} -O defects [75]. Also, dopamine has two main functions. The adhesive nature and controllable growth kinetics of PDA makes it possible to form its conformal layer with controlled thickness on TiO_2 nanoparticles as well as MG sheets [31,76], which can result in a strong connection between MG sheet and TiO_2 . Secondly, dopamine is believed to possess a good redox reactivity which enables localized reduction and fast electronic delivery [77,78]. With these two unique properties, dopamine wrapping onto the surface of $\text{TiO}_2\text{@MG}$ can enhance the electrons transfer between catalyst interfaces, and thus led to its increased photocatalytic activity reported in this work.

To investigate the variations of energy band gap and surface property of anatase TiO_2 and its N-doped sample, model of nitrogen-doped anatase TiO_2 (001) surface ($\text{TiO}_2\text{@MG-D}$) and $\text{H-TiO}_2\text{@MG-D}$ were built based on anatase TiO_2 (001) perfect surface using previously reported method [79,80]. Nitrogen atom doping was assumed to substitute oxygen atom on anatase TiO_2 (001) surface (Fig. S9) resulting in Ti-N. Fig. 14 compares the density of states (DOS) of intrinsic TiO_2 and $\text{TiO}_2\text{@MG-D}$ (001) surface. The calculated values of the minimum energy gap were 2.149, 1.946 and 1.929 eV for perfect TiO_2 , $\text{TiO}_2\text{@MG-D}$ and $\text{H-TiO}_2\text{@MG-D}$, respectively. Fig. 14 suggests that TiO_2 nano-

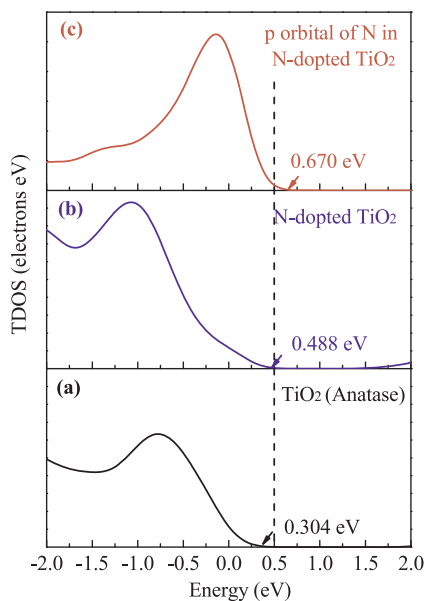


Fig. 14. DOS of: (a) intrinsic anatase TiO_2 , (b) N-doped anatase TiO_2 , and (c) p orbital of N (001) surface.

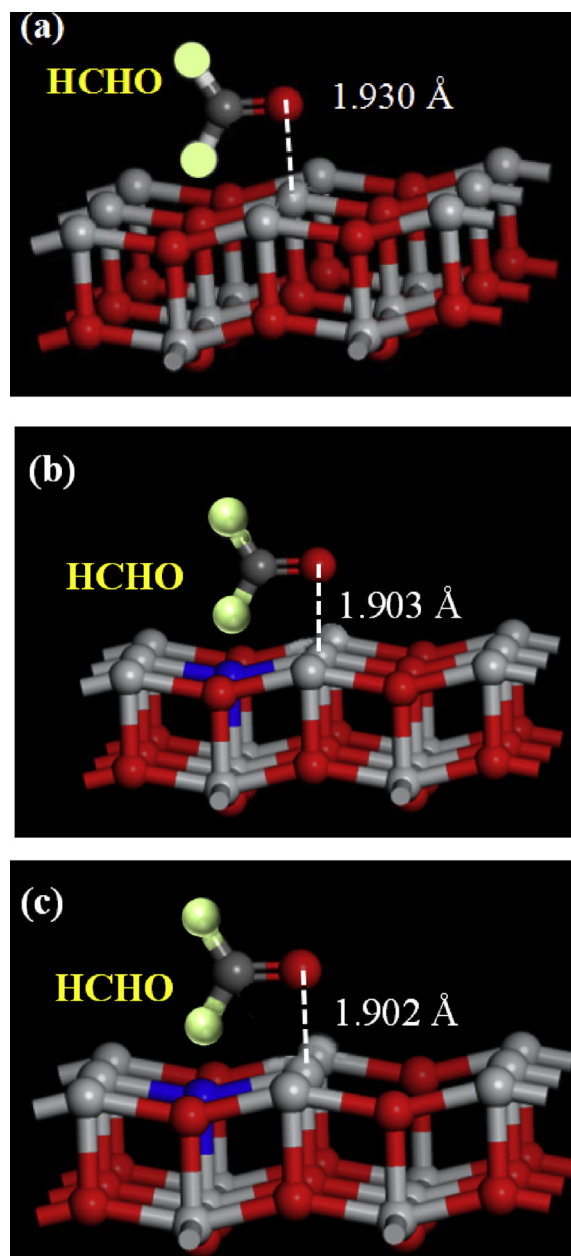


Fig. 15. DOS of: (a) anatase TiO_2 , (b) $\text{TiO}_2\text{@MG-D}$, and (c) $\text{H-TiO}_2\text{@MG-D}$ on (001) surface after HCHO adsorption.

clusters were chemically bonded with N-doped graphene matrix rather than physically adsorbed. Nitrogen incorporated into the lattices of TiO_2 microcrystals gave rise to the boundary of VB due to hybridization of “p” orbital of nitrogen and oxygen in TiO_2 [29], and thus reduced the energy gap. Also, oxygen vacancy of reduced $\text{TiO}_2\text{@MG-D}$ can decrease the energy gap of TiO_2 to 1.929. These simulation results are consistent with XPS data (Fig. 8) and UV-vis DRS (Fig. 9), conforming the assumption of enhanced charge separation efficiency of N-doped TiO_2 by H_2 reduction.

3.3.2. Formaldehyde adsorption-degradation mechanism on N-doped TiO_2 composites

In the current reaction system, the degradation of formaldehyde is assumed to be controlled by synergism of adsorption and photocatalysis. Fig. 15 and Table 2 show the stable adsorption models of formaldehyde on TiO_2 and its composites and calculated parameters, respectively. Formaldehyde molecule can be captured and adsorbed on

Table 2
Comparison of gaseous HCHO degradation activities on as-prepared TiO₂ composite.

Catalyst	S_{BET} (m ² /g)	η^a (%)	k^b (10 ^{−3} min ^{−1})
TiO ₂	163	18	1.48
H-TiO ₂	138	50	4.05
H-TiO ₂ @G	189	76	10.78
H-TiO ₂ @MG	194	80	11.63
H-TiO ₂ @MG-D	184	92	15.04

^a Degradation rate of formaldehyde.

^b Room temperature.

Table 3
DOS parameters of pristine and modified anatase TiO₂ (001) surfaces after HCHO vapors adsorption.

Mode	Ti–O (HCHO) bond length (Å)	Adsorption energy (eV)	Adsorption energy (kJ/mol)
Anatase TiO ₂	1.930	−1.373	−132.3
N-doped TiO ₂	1.903	−1.178	−113.5
H ₂ reduced N- doped TiO ₂	1.902	−1.197	−115.3

TiO₂ (001) surface through strong O(HCHO)–Ti(TiO₂) bond (Fig. 15a) with calculated adsorption energy and adsorption distance as −1.373 eV (132 kJ/mol) and 1.930 Å, respectively. After N doping, adsorption energy of TiO₂ lattice experienced slight decline of 17–19 kJ/mol (Fig. 15b, c), but still fell in the range of chemical adsorption [81]. Ti⁴⁺ in anatase TiO₂ structure acts as a strong acid center with high affinity towards HCHO [82]. In the current set up, formaldehyde was degraded into CO₂ and H₂O. The adsorption site was transferred from basic site (N groups) rather than Ti⁴⁺ (acidic site), which was beneficial in emancipating catalytic active sites (Ti⁴⁺) for the next HCHO adsorption step.

Based on the characterization and simulation results, a proposed mechanism for photocatalytic degradation of HCHO over H-TiO₂@MG-D is illustrated in Fig. 16. UV light irradiation generated excited electrons in nano-structured TiO₂ which were quickly transferred to the highly conducting MG sheets via DA bridged layer [63]. The adsorbed

HCHO on MG sheet surface was readily degraded into intermediate product (HCOOH) and final product as CO₂ (Fig. S8). In brief, the DA wrapping bridge concurrently enhanced the carriers transfer on the interface of TiO₂ and MG sheets and suppressed the recombination of photo-generated electrons and holes. Besides, the decline of energy gap and enhanced basic sites after N-doping also promoted the efficient degradation of HCHO. The synergistic strategy of N-doping and N-wrapping facilitated charge carriers' separation and transfer due to the enhanced interfacial contact of DA bridged TiO₂ and MG sheets and improved electrical conductivity by MG support and DA nano-layer.

4. Conclusions

In summary, we successfully fabricated novel DA bridged melamine-graphene/TiO₂ nano-capsules (H-TiO₂@MG-D) with high photocatalytic degradation activity for gaseous HCHO. Nano-structured TiO₂ was *in situ* grown on the surface of MG support with large 2D π - π network, and was then wrapped by DA nano-layer, forming a MG supported TiO₂ nano-capsule (H-TiO₂@MG-D). Coupling with MG enhanced electrical conductivity, affinity towards HCHO, and decreased the energy gap of TiO₂, resulting in improved photocatalytic activity. In addition, wrapping with DA on the surface of TiO₂ enhanced interfacial contact between TiO₂ and MG sheets, thus promoting the separation and mobility of photoinduced electrons and holes in H-TiO₂@MG-D. Under the synergistic effect of N-doping (melamine modified graphene) and N-wrapping (DA wrapped TiO₂), H-TiO₂@MG-D nano-capsule exhibited the lowest band gap, highest charges separation efficiency and maximum active species ($\cdot\text{O}_2^-$ and $\cdot\text{OH}$) resulting in the highest HCHO photo-degradation activity with fastest reaction rate ($\eta = 92\%$ and $k = 15.04 \times 10^{-3} \text{ min}^{-1}$, respectively). Simulation results indicated that the adsorption sites shifted from acidic Ti⁴⁺ (HCHO) to basic N sites (CO₂) before and after HCHO degradation reaction. This study based on N-doping and N-wrapping as well as bridging strategy can be thought of great promise for various photocatalytic applications in environmental pollution abatements.

Notes

The authors declare no competing financial interest.

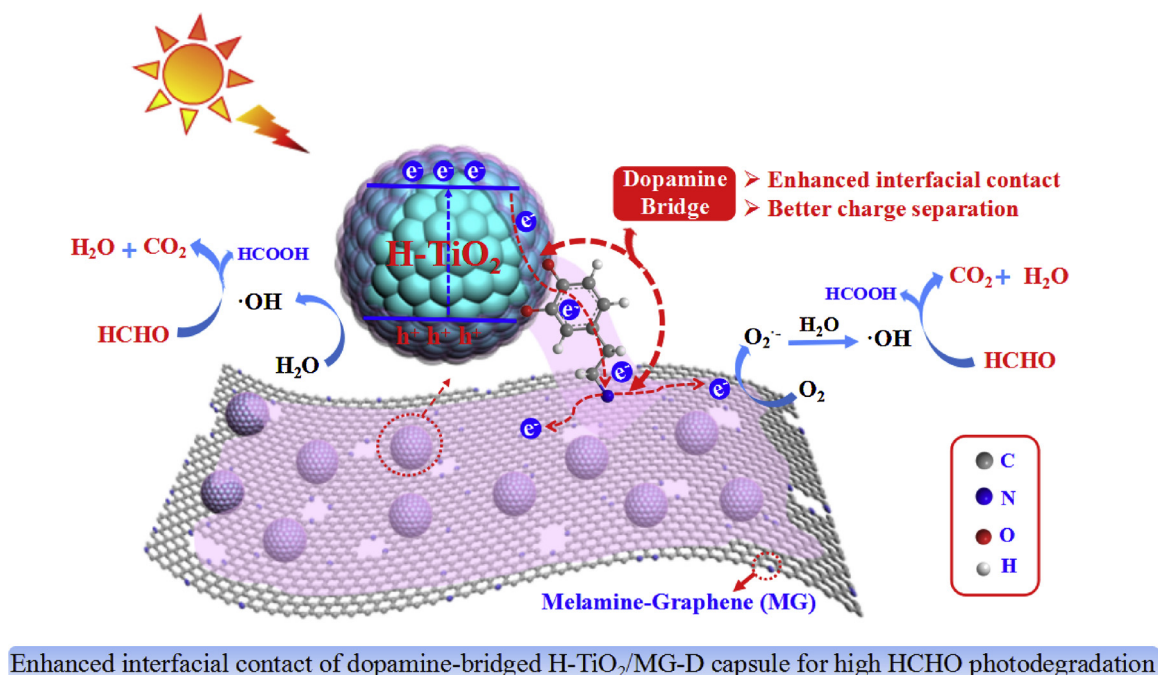


Fig. 16. Schematic illustrations for dopamine bridged Melamine-Graphene/TiO₂ nanocapsule and photocatalytic degradation process of HCHO.

Acknowledgments

This work was financially supported by the National Natural Science Foundation of China (No. 21466003 & 21666004), and Natural Science Foundation of Guangxi Zhuang Autonomous Region, China (Nos. 2017GXNSFFA198009 and 2016GXNSFAA380229), Scientific Research Foundation of Guangxi University (No. XGZ130963), Guangxi Graduate Student Education Innovation Project (No. YCBZ2017010) and Innovation and Entrepreneurship Training Program of Guangxi Zhuang Autonomous Region (No. 201710593185).

Appendix A. Supplementary data

Supplementary material related to this article can be found, in the online version, at doi:<https://doi.org/10.1016/j.apcatb.2018.03.061>.

References

- [1] M.R. Ras, R.M. Marce, F. Borrell, *Sci. Total Environ.* 407 (2009) 4312–4319.
- [2] L. Nie, J. Yu, M. Jaroniec, F.F. Tao, *Catal. Sci. Technol.* 6 (2016) 3649–3669.
- [3] J. Yu, S. Wang, J. Low, W. Xiao, *Phys. Chem. Chem. Phys.* 15 (2013) 16883–16890.
- [4] M. Zamir, R. Halladj, M. Saber, M. Ferdowsi, B. Nasernejad, *Clean: Soil Air Water* 39 (2011) 813–819.
- [5] Z. Zhao, S. Wang, Y. Yang, X. Li, J. Li, Z. Li, *Chem. Eng. J.* 259 (2015) 79–89.
- [6] W.M. Moe, W. Hu, T.A. Key, K.S. Bowman, *Biodegradation* 24 (2013) 685–698.
- [7] P. Dwivedi, V. Gaur, A. Sharma, N. Verma, *Sep. Purif. Technol.* 39 (2004) 23–37.
- [8] Q. Huang, S. Tian, D. Zeng, X. Wang, W. Song, Y. Li, W. Xiao, C. Xie, *ACS Catal.* 3 (2013) 1477–1485.
- [9] D. Sun, L. Ye, Z. Li, *Appl. Catal. B: Environ.* 164 (2015) 428–432.
- [10] J. Du, X. Lai, N. Yang, J. Zhai, D. Kisailus, F. Su, D. Wang, L. Jiang, *ACS Nano* 5 (2011) 590–596.
- [11] Z. Lu, L. Zeng, W. Song, Z. Qin, D. Zeng, C. Xie, *Appl. Catal. B: Environ.* 202 (2017) 489–499.
- [12] H. Wu, X. Wu, Z. Wang, H. Aoki, S. Kutsuna, K. Jimura, S. Hayashi, *Appl. Catal. B: Environ.* 207 (2017) 255–266.
- [13] R. Daghrir, P. Drogui, D. Robert, *Ind. Eng. Chem. Res.* 52 (2013) 3581–3599.
- [14] S.K. Cushing, F. Meng, J. Zhang, B. Ding, C.K. Chen, C. Chen, R. Liu, A.D. Bristow, J. Bright, P. Zheng, N. Wu, *ACS Catal.* 7 (2017) 1742–1748.
- [15] Y. Xu, Y. Mo, J. Tian, P. Wang, H. Yu, J. Yu, *Appl. Catal. B: Environ.* 181 (2016) 810–817.
- [16] H. Diker, C. Varlikli, K. Mizrak, A. Dana, *Energy* 36 (2011) 1243–1254.
- [17] X. Li, P. Liu, Y. Mao, M. Xing, J. Zhang, *Appl. Catal. B: Environ.* 164 (2015) 352–359.
- [18] C. Xue, X. Yan, H. An, H. Li, J. Wei, G. Yang, *Appl. Catal. B: Environ.* 222 (2018) 157–166.
- [19] C. Xue, H. Li, H. An, B. Yang, J. Wei, G. Yang, *ACS Catal.* 8 (2018) 1532–1545.
- [20] F. Pei, S. Xu, W. Zuo, Z. Zhang, Y. Liu, S. Cao, *Int. J. Hydrogen Energy* 39 (2014) 6845–6852.
- [21] C. Xue, H. An, X. Yan, J. Li, B. Yang, J. Wei, G. Yang, *Nano Energy* 39 (2017) 513–523.
- [22] B. Qiu, M. Xing, J. Zhang, *J. Am. Chem. Soc.* 136 (2014) 5852–5855.
- [23] B. Lin, H. An, X. Yan, T. Zhang, J. Wei, G. Yang, *Appl. Catal. B: Environ.* 210 (2017) 173–183.
- [24] B. Lin, H. Li, H. An, W. Hao, J. Wei, Y. Dai, C. Ma, G. Yang, *Appl. Catal. B: Environ.* 220 (2018) 542–552.
- [25] B. Lin, G. Yang, B. Yang, Y. Zhao, *Appl. Catal. B: Environ.* 198 (2016) 276–285.
- [26] D.C. Marcano, D.V. Kosynkin, J.M. Berlin, A. Sinitskii, Z. Sun, A. Slesarev, L.B. Alemany, W. Lu, J.M. Tour, *ACS Nano* 4 (2010) 4806–4814.
- [27] L. Zhang, Q. Zhang, H. Xie, J. Guo, H. Lyu, Y. Li, Z. Sun, H. Wang, Z. Guo, *Appl. Catal. B: Environ.* 201 (2017) 470–478.
- [28] M.D. Segall, P.J.D. Lindon, M.J. Probert, C.J. Pickard, P.J. Hasnip, S.J. Clark, M.C. Payne, *J. Phys. Condens. Mater.* 14 (2002) 2717.
- [29] X. Dong, X. Zhang, H. Cui, J. Zhang, *Appl. Surf. Sci.* 422 (2017) 331–338.
- [30] John P. Perdew, Y. Wang, *Phys. Rev. B* 45 (1992) 13244–13249.
- [31] W. Mao, X. Lin, W. Zhang, Z. Chi, R. Lyu, A. Cao, L. Wan, *Chem. Commun.* 52 (2016) 7122–7125.
- [32] H. Zhang, L. Guo, D. Wang, L. Zhao, B. Wan, *ACS Appl. Mater. Interfaces* 7 (2015) 1816–1823.
- [33] K. Chang, W. Chen, *ACS Nano* 5 (2011) 4720–4728.
- [34] M.C. Daniel, D. Astruc, *Chem. Rev.* 104 (2004) 293–346.
- [35] J. Zhang, J. Yu, Y. Zhang, Q. Li, J.R. Gong, *Nano Lett.* 11 (2011) 4774–4779.
- [36] X. Zhou, B. Jin, J. Luo, X. Xu, L. Zhang, J. Li, H. Guan, *RSC Adv.* 6 (2016) 64446–64449.
- [37] L. Zhang, H. Fu, Y. Zhu, *Adv. Funct. Mater.* 18 (2008) 2180–2189.
- [38] M. Zhu, K. Zhou, X. Sun, Z. Zhao, Z. Tong, Z. Zhao, *Chem. Eng. J.* 317 (2017) 660–672.
- [39] L. Sang, Y. Zhao, C. Burda, *Chem. Rev.* 114 (2014) 9283–9318.
- [40] S. Wang, H. Niu, T. Zeng, X. Ma, Y. Cai, X. Zhao, *CrystEngComm* 16 (2014) 5598–5607.
- [41] W. Zhang, X. Jiang, Y. Zhao, A. Carne-Sanchez, V. Malgras, J. Kim, J.H. Kim, S. Wang, J. Liu, J. Jiang, Y. Yamauchi, M. Hu, *Chem. Sci.* 8 (2017) 3538–3546.
- [42] Y. Xu, Y. Zhuang, X. Fu, *J. Phys. Chem. C* 114 (2010) 2669–2676.
- [43] G. Zhang, Y.C. Zhang, M. Nadagouda, C. Han, K. O'Shea, S.M. El-Sheikh, A.A. Ismail, D.D. Dionysiou, *Appl. Catal. B: Environ.* 144 (2014) 614–621.
- [44] T. Leshuk, R. Parviz, P. Everett, H. Krishnakumar, R.A. Varin, F. Gu, *ACS Appl. Mater. Interfaces* 5 (2013) 1892–1895.
- [45] M.S.A.S. Shah, A.R. Park, K. Zhang, J.H. Park, P.J. Yoo, *ACS Appl. Mater. Interfaces* 4 (2012) 3893–3901.
- [46] M. Zhu, Z. Tong, Z. Zhao, Y. Jiang, Z. Zhao, *Ind. Eng. Chem. Res.* 55 (2016) 3765–3774.
- [47] F.M. Hoffmann, R.A. de Paola, *Phys. Rev. Lett.* 52 (1984) 1697.
- [48] T. Sun, J. Song, J. Jia, X. Li, X. Sun, *Nano Energy* 26 (2016) 83–89.
- [49] F. Chen, S. Liu, J. Yu, *Phys. Chem. Chem. Phys.* 18 (2016) 18161–18168.
- [50] H. Sui, F. Zhong, K. Cheng, X. Liu, X. Ju, *Spectrochim. Acta A* 114 (2013) 137–143.
- [51] M. Colella, G.R. Lumpkin, Z. Zhang, E.C. Buck, K.L. Smith, *Phys. Chem. Miner.* 32 (2005) 52–64.
- [52] A. Baranov, S. Fanchenko, L. Calliari, G. Speranza, L. Minati, A.V. Shorokhov, D. Fedoseenkov, A. Nefedov, *Diam. Relat. Mater.* 16 (2007) 1365–1369.
- [53] C. Chen, Y. Wen, X. Hu, X. Ji, M. Yan, L. Mai, P. Hu, B. Shan, Y. Huang, *Nat. Commun.* 6 (2015).
- [54] P. Xia, B. Zhu, J. Yu, S. Cao, M. Jaroniec, *J. Mater. Chem. A* 5 (2017) 3230–3238.
- [55] Q. Chang, L. Liu, M. Yaseen, S. Weng, Z. Feng, T. Wei, J. Lei, Z. Tong, Z. Zhao, *Chem. Eng. J.* 334 (2018) 1699–1708.
- [56] Y. Wei, Y. Wu, Q. Chang, M. Xie, X. Wang, J. Mo, X. He, Z. Zhao, Z. Zhao, *RSC Adv.* 7 (2017) 35159.
- [57] M. Tao, H. Sun, L. Liu, X. Luo, G. Lin, R. Li, Z. Zhao, Z. Zhao, *J. Agric. Food Chem.* 65 (2017) 8626–8633.
- [58] X. He, H. Sun, M. Zhu, M. Yaseen, D. Liao, X. Cui, H. Guan, Z. Tong, Z. Zhao, *Chem. Commun.* 53 (2017) 3442–3445.
- [59] B. Chai, T. Peng, J. Mao, K. Li, L. Zan, *Phys. Chem. Chem. Phys.* 14 (2012) 16745–16752.
- [60] X. Cui, S. Yang, X. Yan, J. Leng, S. Shuang, P.M. Ajayan, Z. Zhang, *Adv. Funct. Mater.* 26 (2016) 5708–5717.
- [61] X. Li, J. Yu, S. Wageh, A.A. Al-Ghamdi, J. Xie, *Small* 12 (2016) 6640–6696.
- [62] N.M. Dimitrijevic, E. Rozhkova, T. Rajh, *J. Am. Chem. Soc.* 131 (2009) 2893–2899.
- [63] F. Xiao, S. Hung, H.B. Tao, J. Miao, H.B. Yang, B. Liu, *Nanoscale* 6 (2014) 14950–14961.
- [64] J. Ran, G. Gao, F. Li, T. Ma, A. Du, S. Qiao, *Nat. Commun.* 8 (2017).
- [65] X. Cai, J. Zhang, M. Fujitsuka, T. Majima, *Appl. Catal. B: Environ.* 202 (2017) 191–198.
- [66] H. Wang, X. Yuan, Y. Wu, G. Zeng, X. Chen, L. Leng, H. Li, *Appl. Catal. B: Environ.* 174 (2015) 445–454.
- [67] S. Cao, J. Low, J. Yu, M. Jaroniec, *Adv. Mater.* 27 (2015) 2150–2176.
- [68] Y. Zhang, Z. Tang, X. Fu, Y. Xu, *ACS Nano* 4 (2010) 7303–7314.
- [69] S. Bingham, W.A. Daoud, *J. Mater. Chem.* 21 (2011) 2041–2050.
- [70] R. Raccichini, A. Varzi, S. Passerini, B. Scrosati, *Nat. Mater.* 14 (2015) 271–279.
- [71] Q. Zhang, W. Wang, J. Yu, D. Qu, H. Tian, *Adv. Mater.* (2017) 29.
- [72] J. Tian, Y. Leng, H. Cui, H. Liu, *J. Hazard. Mater.* 299 (2015) 165–173.
- [73] Q. Xiang, B. Cheng, J. Yu, *Angew. Chem. Int. Ed.* 54 (2015) 11350–11366.
- [74] P. Hu, X. Liang, M. Yaseen, X. Sun, Z. Tong, Z. Zhao, Z. Zhao, *Chem. Eng. J.* 332 (2017) 608–618.
- [75] V.V. Gorodetskii, A.A. Sametova, A.V. Matveev, V.M. Tapilin, *Catal. Today* 144 (2009) 219–234.
- [76] J. Zhou, P. Wang, C. Wang, Y.T. Goh, Z. Fang, P.B. Messersmith, H. Duan, *ACS Nano* 9 (2015) 6951–6960.
- [77] K.C.L. Black, Z. Liu, P.B. Messersmith, *Chem. Mater.* 23 (2011) 1130–1135.
- [78] L. Zhang, J. Wu, Y. Wang, Y. Long, N. Zhao, J. Xu, *J. Am. Chem. Soc.* 134 (2012) 9879–9881.
- [79] J. Yu, G. Dai, Q. Xiang, M. Jaroniec, *J. Mater. Chem.* 21 (2011) 1049–1057.
- [80] M. Khan, J. Xu, N. Chen, W. Cao, *J. Alloys Compd.* 513 (2012) 539–545.
- [81] H.T.T. Tran, M.J.S. Spencer, *Mater. Chem. Phys.* 193 (2017) 274–284.
- [82] P.R. McGill, H. Idriss, *Langmuir* 24 (2008) 97–104.